

Effects of signal corrections on measurements of temperature and OH concentrations using laser-induced fluorescence

Zhiyao Yin · Campbell D. Carter · Walter R. Lempert

Received: 12 December 2013 / Accepted: 18 June 2014 / Published online: 10 July 2014
© Springer-Verlag Berlin Heidelberg 2014

Abstract Temperature and OH concentrations derived from OH laser-induced fluorescence (LIF) are known to be susceptible to effects such as collisional quenching, laser absorption, and fluorescence trapping. In this paper, a set of analytical and easy-to-implement methods is presented for treating these effects. The significance of these signal corrections on inferred temperature and absolute OH concentration is demonstrated in an atmospheric-pressure, near-stoichiometric CH₄-air flame stabilized on a Hencken burner, for laser excitation of both the A²Σ⁺ ← X²Π (0,0) and (1,0) bands. It is found that the combined effect of laser attenuation and fluorescence trapping can cause considerable error in the OH number density and temperature if not accounted for, even with A–X(1,0) excitation. The validity of the assumptions used in signal correction (that the excited-state distribution is either thermalized or frozen) is examined using time-dependent modeling of the ro-vibronic states during and after laser excitation. These assumptions are shown to provide good bounding approximations for treating transition-dependent issues in OH LIF, especially for an unknown collisional environment, and it is noted that the proposed methods are generally applicable to LIF-based measurements.

1 Introduction

With a long history of development, laser-induced fluorescence (LIF) has been widely employed in the detection of the hydroxyl radical (OH), an important intermediate species in combustion [1], atmospheric chemistry [2] and plasmas [3]. Despite the abundant information available on the spectroscopic characteristics of the OH molecule and the availability of the laser sources for various excitation schemes, absolute OH number density measurement by LIF remains challenging in many circumstances. Likewise, accurate thermometry based on multi-line OH LIF is both attractive—for these same reasons—and difficult.

One obstacle encountered in quantitative OH LIF for either temperature or concentration measurement is associated with the determination of fluorescence quantum yield, which depends on various energy transfer processes during and after laser excitation, such as radiative decay, rotational energy transfer (RET), vibrational energy transfer (VET), and electronic quenching. Despite some successes modeling temperature-dependent quenching of OH A²Σ⁺ (the excitation destination of most OH LIF techniques) [4, 5], comprehensive theories do not yet exist for describing all aspects of the major collisional processes (i.e., RET, VET, and quenching), such as their dependence on temperature (*T*), rotational level in the excited state (*J'*), and collision partners (e.g., air constituents, hydrocarbons, radicals, and excited species). To account for these issues in data analysis, one common practice is to rely on (1) reported collisional cross sections, measured mostly at ≤300 K [6–8] and at flame temperatures [9–12] for OH A²Σ⁺ (*v'* = 1 and 0) and/or (2) empirical relations describing their *J'*- and *T* dependencies [13–16], assuming that temperature and gas composition in the probe volume are known. Alternatively, the total rate of quenching/VET for a specific probe volume

Z. Yin (✉) · W. R. Lempert
Michael A. Chaszeyka Nonequilibrium Thermodynamics
Laboratories, Department of Mechanical Engineering,
The Ohio State University, W090 Scott Lab, 201. W 19th Ave,
Columbus, OH 43210, USA
e-mail: yin.67@osu.edu

C. D. Carter
Air Force Research Laboratory, Wright-Patterson AFB, Dayton,
OH 45433, USA

may be obtained by direct measurement of OH lifetime, provided that the fluorescence decay can be properly resolved by the laser pulse and the detection system [14].

Other issues in extracting quantitative information from LIF may be encountered in the evaluation of the efficiency of the experimental setup, mainly including considerations of laser beam attenuation, fluorescence trapping, and the optical efficiency of the detection system. In systems with high OH average concentration and/or large spatial scales, the laser beam may experience attenuation as it traverses the environment. Fluorescence may also be reabsorbed along the signal collection path, a process known as *fluorescence trapping*. Both issues can introduce considerable error if neglected, depending on the OH number density, line strength of the excitation transition, and the sampling location. Although it is a common practice nowadays to consider laser attenuation, much less attention is paid to fluorescence trapping due to the lack of a general approach for its treatment. By a combination of (1,0) excitation of OH $A^2\Sigma^+ \leftarrow X^2\Pi$ and collection of (1,1) emission, trapping may be largely avoided (though at the cost of increased sensitivity to VET). However, as the (1,1) band overlaps with the (0,0) band, it is difficult to isolate either band without spectrally resolving the fluorescence, which is impractical for certain applications such as planar imaging.

To derive absolute OH number density, it is necessary to determine the optical efficiency of the detection system, generally consisting of windows, focusing lenses, optical filters (or a monochromator), and a photon detector (e.g., a photomultiplier tube, PMT, or a charge-coupled device, CCD). Instead of direct calculation, the collective optical efficiency of the detection system is often deduced via calibration. Previously demonstrated calibration techniques include signal comparison with an external reference flame (such as a Hencken burner [17] where the concentration is known) or with Rayleigh/Raman scattering. The reference flame approach, albeit straightforward, may introduce significant error if (1) the concentration is not well known [18], (2) the same optical alignment for the flame and for the target system is not guaranteed, and/or (3) the collisional environment at the condition of interest is significantly different from that of the calibration environment. On the other hand, laser scattering-based techniques make possible the use of the same test facility for both LIF and calibration, such as shown in some early demonstrations for calibrating CH and OH LIF in flames using Rayleigh [19–21] and Raman scattering (Stokes radiation) [19, 22]. Spontaneous Raman scattering may prove advantageous for nonresonant detection in situations where Rayleigh calibration using the same excitation laser frequency would require additional corrections for spectral bias of the detection system.

It is worth pointing out that over the years, approaches have emerged for OH LIF to mitigate the aforementioned issues:

collision-insensitive techniques such as *saturated LIF* [20, 21], and the combination of picosecond excitation and narrow-gate collection [23] have been used to obviate the need for quenching corrections. A bidirectional laser beam configuration has been demonstrated to be collision independent and self-calibrated for absolute OH number density measurements [24]. In spite of their obvious advantages, these techniques may demand complicated modeling of the excitation/fluorescence process [20] or additional experimental complexity and may not be amenable to measurements in turbulent flames.

In this work, we examine in detail possible uncertainties and systematic errors associated with temperature and absolute concentration measurements for the most common approach of OH LIF setup, i.e., linear excitation in the (1,0) or (0,0) band of OH $A^2\Sigma^+ \leftarrow X^2\Pi$ and broadband detection of fluorescence, in an atmospheric-pressure flame generated by a Hencken burner. Our goal is to present viable and easy-to-use analytical solutions for treating transition-dependent laser attenuation, fluorescence yield, and fluorescence trapping. In addition, the accuracy and efficacy of Rayleigh scattering-based calibration of the fluorescence signal is determined by comparison to laser absorption measurements. To our knowledge, this comparison has been done only for saturated LIF measurements [20], wherein the approach and challenges differ significantly from linear LIF. The importance of the various corrections/treatments is seen by comparing (1) the OH LIF-based temperature to the expected temperature (from equilibrium considerations) and (2) the Rayleigh scattering-calibrated number density to the value from absorption. With regard to concentration measurements, these corrections are relevant to the use of any LIF calibration factor (i.e., in *transferring* the calibration from one condition to another), regardless of its origin.

2 Experimental

In this work, a 25-mm-square Hencken burner (Technologies for Research, model RD1X1), as illustrated (top view) in Fig. 1, was used for OH absorption and OH LIF/Rayleigh calibration measurements. Unlike a standard model that operates in nonpremixed mode, this burner was modified to operate in a premixed mode only (i.e., it did not include the fuel tubes). A near-stoichiometric mixture (equivalence ratio $\phi \sim 0.95$) of CH_4 (1.0 standard liters per minute, SLPM, with standard conditions of 1 standard atmosphere and 273.15 K) and air (9.6 SLPM) was delivered through the main flow region, as shown in Fig. 1. The CH_4 (Grade 2.0) was of 99 % purity. A coalescing filter (Balston A912A-DX) was used to remove water vapor and oil particles in the compressed air before it was mixed with CH_4 . The flow rates were metered by Tylan mass flow controllers, which were calibrated using a Bios Drycal

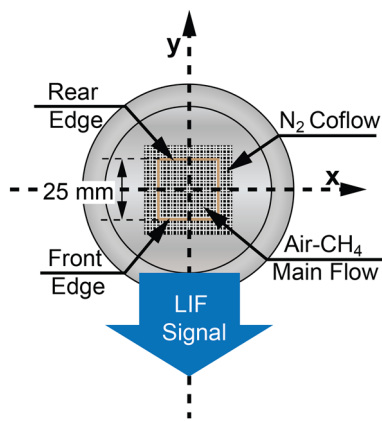


Fig. 1 Illustration (not to scale) of the Hencken burner (*top view*) used in this work

piston-type device prior to the experiment. N_2 was supplied in the co-flow region at a total flow rate similar to the main flow, to reduce buoyancy-induced flame instability.

The experiments described in this work were carried out collaboratively at the Air Force Research Laboratory (AFRL) and The Ohio State University (OSU). At AFRL, combined OH LIF and absorption measurements were used to determine the absolute OH number density in the Hencken flame. For that, an injection-seeded Nd:YAG laser (Spectra Physics GCR-170) was used to pump a tunable dye laser (Lumonics Hyperdye 300). The dye laser output (near 619 nm) was frequency doubled within an Inrad Autotracker III; the UV beam was separated from the dye beam within an Inrad Prism Harmonic Separator (PHS), attenuated to about 1 $\mu\text{J}/\text{pulse}$, and then softly focused using a 1-m focal length lens. The laser beam was aligned to probe 25 mm above the burner surface, where near equilibrium conditions were estimated to have been achieved. The 309-nm laser beam has a pulse width of 8 ns and an estimated linewidth of $\sim 0.2 \text{ cm}^{-1}$. Beam energies before and after the flame were recorded using Molectron Joulemeters coupled to integrating spheres; the purpose of the integrating sphere is to remove all spatial information from the beam (before being sampled by the Joulemeter). Joulemeter signals were recorded using a digital oscilloscope (LeCroy Waverunner HRO 64Zi with 12-bit resolution) using a correlated double sampling approach. The relative noise levels between the two signals were typically $\sim 0.05 \%$. Using a PIMAX camera, the OH profile along the laser line was imaged via LIF synchronously with absorption to derive the absorption path length (for each absorption measurement):

$$L_{\text{abs}}(x = a) = \frac{1}{S_f(x = a)} \int_{-Ax}^{Ax} S_f(x) dx. \quad (1)$$

In Eq. (1), $S_f(x)$ is the LIF signal at location x (refer to Fig. 1 for the naming convention of the burner dimensions); a is

the calibration location, and the integration limits Δx were chosen to encompass the entire OH profile. For these measurements, the calibration location was at the center of the burner (i.e., $x = 0$ as shown in Fig. 1). Since the profile should represent the OH number density (from a specific rotational ground state), main-branch transitions could not be used, due to laser attenuation (and the corresponding distortion of the OH profile). Thus, satellite transitions, which suffer minimal distortion from attenuation as the laser traverses the flame, were employed to derive L_{abs} .

At OSU, OH concentration and rotational temperature were measured by OH LIF in the near equilibrium CH_4 -air flame with the same Hencken burner (shown in Fig. 1) and flow control system used at AFRL. A similar UV generation setup was used, which consists of an Nd:YAG (Continuum, Model Powerlite 8010), a dye laser (Laser Analytical Systems, Model LDL 20505), an Inrad Auto-tracker II and a PHS. The UV laser beam has a pulse width of 10 ns and an estimated linewidth of $\sim 0.75 \text{ cm}^{-1}$. The UV laser energy was measured by a power meter (Model P09, Scientech) and monitored during the experiment by a photodiode (Thorlabs Model DET210). To insure operation in the linear excitation regime, the laser energy was attenuated down to ~ 0.1 – $1.0 \mu\text{J}/\text{pulse}$. The fluorescence was collimated and focused into a photomultiplier tube (PMT); filters were mounted at the entrance of the PMT housing, including colored glasses (Schott UG 11 and in certain cases WG305) and a neutral density filter ($\text{OD} = 0.4$, Newport). An entrance slit on the PMT housing was used to limit the sampling volume to be about 3-mm long (from $x = -1.5 \text{ mm}$ to $x = 1.5 \text{ mm}$) and 1.5-mm tall. The entire LIF pulse was integrated and stored in real time using a digital oscilloscope (LeCroy, WAVEPRO 7100A). Rayleigh scattering at the fluorescence wavelength ($\sim 308 \text{ nm}$) was used to calibrate the relative OH signal, the details of which will be presented in Sect. 4.

3 Laser absorption measurements

OH absorbance was measured by scanning across both $Q_1(9.5)$ (and the satellite $P_{21}(9.5)$) and $Q_2(6.5)$ (and the satellite $R_{12}(6.5)$) transitions in the OH $A^2\Sigma^+ \leftarrow X^2\Pi$ ($v' = 0, v'' = 0$) band. The absolute OH number density, n_{OH} , can then be derived iteratively as follows:

$$\begin{aligned} &\text{Integrated Experimental Absorbance} \\ &= \int_{-Ax}^{+Ax} \{1 - \exp[-hv_0 g_a(v, v_0, T, P) f_B n_{\text{OH}} L_{\text{abs}}(x) b_{lu}]\} dv, \end{aligned} \quad (2)$$

where h is the Planck constant (J·s); v_0 is center of the transition (cm^{-1}); f_B is the Boltzmann factor for OH

molecules in the absorbing state, calculated using the rotational term energies for $X^2\Pi v = 0$ state from Coxon [25]; n_{OH} is OH number density (cm^{-3}); $b_{\text{lu}} = B_{\text{lu}}/c$ is the Einstein absorption coefficient ($\text{cm}^2 \text{J}^{-1} \text{cm}^{-1}$), taken from LIFBASE [26]; g_a is the normalized absorption lineshape and is a convolution of the collisional broadening lineshape and the Doppler lineshape. The collision broadening linewidth was calculated based on the experimental results reported by Rea et al. [27, 28]. Since Doppler broadening dominates the absorption lineshape at atmospheric flame conditions, the uncertainty introduced by the estimated collisional broadening is likely small. The limits for spectral integration, $\pm\Delta\nu$, were chosen to include the entire experimental absorbance as much as possible. The measured absorption path length for the corresponding transition and an assumed temperature of 2,150 K were used in the exponential term in Eq. (2). Since the ground-state populations for both main-branch transitions chosen here are temperature insensitive in the range of 1,500–2,500 K (especially for $J'' = 9.5$), the error introduced by the assumed temperature is negligible.

For the set of 12 measurements performed at the center of the flame ($y = 0$ mm), 25 mm from the surface ($z = 25$ mm), the average n_{OH} was $(0.916 \pm 0.006) \times 10^{16} \text{ cm}^{-3}$, with the given uncertainty being the standard deviation of the 12 measurements. As a check, absorption and path length measurements were repeated using (1,0) transitions; the derived concentration among 12 measurements was slightly higher, equaling $(0.943 \pm 0.008) \times 10^{16} \text{ cm}^{-3}$. These values are consistent with an equilibrium OH number density at 2,170 K (vs. an adiabatic value of about 2,190 K). A set of absorption scans was also performed at 5 mm from the front edge of the burner ($y = -7$ mm), employing the OH profile obtained at this location. n_{OH} at this location was determined to be $0.71 \times 10^{16} \text{ cm}^{-3}$, approximately equal to the equilibrium value at 2,100 K. Considering the various sources of uncertainty (T , L_{abs} , b_{lu} , collisional broadening, etc.), the overall relative uncertainty of $n_{\text{OH,abs}}$ is estimated to be $\pm 6\%$ and thus at the center of the flame $n_{\text{OH,abs}}$ ($x = 0$, $y = 0$, $z = 25$ mm) = $(0.93 \pm 0.05) \times 10^{16} \text{ cm}^{-3}$, and likewise at the edge of the flame, $n_{\text{OH,abs}}$ ($x = 0$, $y = -7$ mm, $z = 25$ mm) = $(0.71 \pm 0.04) \times 10^{16} \text{ cm}^{-3}$. It is noted that

this easily repeatable flame condition and corresponding OH concentration can be used by those interested in calibrating OH LIF.

4 Signal corrections for OH LIF

4.1 Transition-dependent quantum yield

Operating in the linear excitation regime, the time-integrated (from 0 to ∞) fluorescence signal, $S_f(\nu_L)$, at the laser frequency ν_L (cm^{-1}), can be expressed as follows:

$$S_f(\nu_L) = n_{\text{OH}} f_B b_{\text{lu}} E \phi_J g(\nu_L) \frac{l \Omega \beta}{4\pi}, \quad (3)$$

where E is the laser energy (J); ϕ_J is the fluorescence quantum efficiency (or quantum yield); $g(\nu_L)$ is the overlap integral ($1/\text{cm}^{-1}$), i.e., a convolution of laser lineshape and absorption lineshape; l is the path length of the laser sampled by the collection optics (cm); Ω is the solid angle of detection (sr); and β represents the overall effectiveness of the detection system for converting incident photons into volts (in the case of a PMT detector coupled with an oscilloscope). For ($v' = 0$, $v'' = 0$) excitation and collection of fluorescence from the $v' = 0$ level, the quantum yield ϕ_J can be expressed generally as:

$$\phi_J = \frac{\sum_{v'=0, J'} f_{J'} \cdot \left(\sum_{v'', J''} \varepsilon_{v'', J''}^{v'=0, J'} \cdot A_{v'', J''}^{v'=0, J'} \right)}{\sum_{v'=0, J'} f_{J'} \cdot (A_{v'=0, J'} + Q_{v'=0, J'})}, \quad (4)$$

where $\varepsilon_{v'', J''}^{v'=0, J'}$ accounts for detection efficiencies (from the PMT and various filters) and fluorescence trapping, both of which may depend on specific transition; $A_{v'', J''}^{v'=0, J'}$ and $A_{v'=0, J'}$ are the transition-dependent and the J' -dependent radiative decay rates, respectively, and are related via $A_{v'=0, J'} = \sum_{v'', J''} A_{v'', J''}^{v'=0, J'}$ (a sum of all possible transitions); $Q_{v'=0, J'}$ is the J' -dependent quenching rate; $f_{J'}$ represents the time-integrated population fraction of J' in $v' = 0$, such that $\sum_{v'=0, J'} f_{J'} = 1$. For ($v' = 1$, $v'' = 0$) excitation and collection of fluorescence from both $v' = 1$ and $v' = 0$, ϕ_J takes the following form by also taking into account J' -dependent VET from $v' = 1$ to $v' = 0$, $V_{10, J'}$:

$$\phi_J = \frac{\sum_{v'=1, J'} f_{J'} \cdot \left(\sum_{v'', J''} \varepsilon_{v'', J''}^{v'=1, J'} \cdot A_{v'', J''}^{v'=1, J'} \right) + \frac{1}{r} \cdot \left[\sum_{v'=0, J'} f_{J'} \cdot \left(\sum_{v'', J''} \varepsilon_{v'', J''}^{v'=0, J'} \cdot A_{v'', J''}^{v'=0, J'} \right) \right] \cdot \left(\sum_{v'=1, J'} f_{v'=1, J'} \cdot V_{10, J'} \right)}{\sum_{v'=1, J'} f_{v'=1, J'} \cdot (A_{v'=1, J'} + Q_{v'=1, J'} + V_{10, J'})}, \quad (5)$$

where $r = \sum_{v'=0, J'} f_{J'} \cdot (A_{v'=0, J'} + Q_{v'=0, J'})$ and upward VET (from $v' = 1$ to $v' = 2$, etc.) is neglected. Note that in this case, $\sum_{v'=0, J'} f_{J'} = 1$ and $\sum_{v'=1, J'} f_{J'} = 1$. To properly evaluate the time-integrated population fraction $f_{J'}$, comprehensive simulation of the laser excitation and various energy transfer processes including radiative decay, RET, VET and electronic quenching among all involved ro-vibrational levels may be necessary. Two extreme cases regarding $f_{J'}$ were first considered: (1) completely thermalized excited-state population, i.e., $f_{J'}$ follows a relative Boltzmann distribution at the flame temperature; (2) *frozen* or *nonthermal* population, i.e., all fluorescence originates from the directly excited J' (no RET). These assumptions, albeit crude, provide limiting cases and are much easier to implement in calculation. Note that these two extreme conditions can be approximated experimentally given proper design (e.g., using Ar/He to enhance RET for fast thermalization of v' [10] or operating at very low pressure to reduce RET for J' dependence study [12]). The validity of using these two assumptions for the atmospheric-pressure Hencken flame will be further addressed in Sect. 7 by comparing them to LIF simulations carried out using the LASKIN program [29].

In this work, individual values of $A_{v', J'}$ (for both $v' = 1$ and $v' = 0$) were taken from LIFBASE. Although several empirical expressions for $Q_{v'=0, J'}$ and $V_{10, J'}$ have been proposed in the literature [14, 16], they are often validated under certain specific flame environments. On the other hand, the total electronic quenching and VET rates (Q_1 , Q_0 and V_{10}) have been measured in similar atmospheric-pressure CH₄-air flames [30, 31]. It has also been reported that quenching by H₂O (accounting for more than 80 % of the total quenching rate in the Hencken flame) becomes nearly J' independent at $T = 2,300$ K [9]. Based on these reported rates and the cross sections for electronic quenching and VET measured in a shock tube (1,900–2,300 K) given in [10, 11], estimated values of $Q_1 \approx Q_0 = 4.9 \times 10^8 \text{ s}^{-1}$ and $V_{10} = 3.0 \times 10^8 \text{ s}^{-1}$ were used for signal corrections using the two bounding assumptions, instead of assuming certain J' dependencies for electronic quenching and VET. Note that for LASKIN simulations, however, empirical relations for $Q_{v'=0, J'}$ and $V_{10, J'}$ were implemented, as described in Sect. 7.

4.2 Spectral bias and fluorescence trapping

As noted earlier, the term ε in Eqs. (4) and (5) concerns possible spectral bias and fluorescence trapping. When accounting for spectral bias, transmittance spectra were obtained (using a UV/Vis spectrometer) for all the colored glass and neutral density filters used in this work. Most filters and the PMT have approximately flat efficiency

profiles across the range of 280–330 nm, in which fluorescence from OH $A^2\Sigma^+ \rightarrow X^2\Pi$ (0,0), (1,0), and (1,1) bands reside (the three most significant emission bands following the excitation to either $v' = 0$ or $v' = 1$). However, the 2-mm thick Schott WG305 filter (commonly used for blocking laser radiation in the case of (1,0) excitation) has a transmittance varying from 50 % at 305 nm to 84 % at 325 nm. Therefore, the (0,0) band (305–316 nm) may be preferentially attenuated (especially for emission from the R-branch) compared with the (1,1) band (312–325 nm). This bias has been taken into account during data analysis when the WG305 filter was used.

On the other hand, treating fluorescence trapping in flames with high OH concentrations is not as straightforward. Quantification of fluorescence trapping requires not only knowledge of OH concentration within each excited ro-vibronic state in the probe volume but also the ground-state OH concentration at each point between the probe volume and the detector. The wavelength dependence of fluorescence trapping has been demonstrated in a recent work wherein fluorescence trapping was measured from spectrally resolved OH LIF and OH* chemiluminescence [32]. Signal attenuation up to 40 % in the presence of an absorber flame was reported, with the most pronounced effect found in emission from the (0,0) band (mainly due to higher population in $v'' = 0$). One obvious remedy for minimizing fluorescence trapping would be to employ (1,0) excitation followed by (1,1) detection. As mentioned in the introduction, this approach is not applicable for quantitative planar imaging, since it is almost impossible to isolate (1,1) band emission from the (0,0) band with commercially available band-pass filters; furthermore, isolation of the (1,1) band fluorescence (from the total) would decrease the LIF signal strength and increase the sensitivity to VET. In cases where quantitative flame properties are extracted from OH* chemiluminescence (such as heat release rate and equivalence ratio sensing [33]), a practical method for quantifying signal trapping would, of course, be helpful.

In this work, we propose the following expression for estimating transition-dependent fluorescence trapping:

$$\text{Tr}_{v', J'}^{v'', J''} = \int_{-4v}^{+4v} \exp[-hv_0 g_a(v, v_0, T, P) f_{B^1\text{OH}} L_{\text{tr}}(y) b_{\text{lu}}] \cdot g_e(v) dv. \quad (6)$$

Equation (6) essentially represents the transmittance of fluorescence along the signal collection path (i.e., along the y -axis of the burner as indicated in Fig. 1). L_{tr} is the effective absorption length that the fluorescence experiences as it travels from the sample volume to the edge of the flame [similar to the definition of L_{abs} in Eq. (1)]. g_e is the emission lineshape, which was assumed to have the same form as g_a (i.e., considering Doppler and collision

broadening). In order to evaluate the use of Eq. (6), fluorescence trapping was measured (at AFRL), utilizing a motorized translation stage (which supports the burner) and the LIF line imaging system described in Sect. 2. The experiments consisted of two steps. First, by translating the burner along its y -axis (refer to Fig. 1), the probe volume of the laser beam can be varied such that the fluorescence signal is subjected to a varying L_{tr} . To guarantee that laser attenuation is insignificant, the satellite $P_{21}(9.5)$ transition in the OH $A^2\Sigma^+ \leftarrow X^2\Pi$ ($v' = 0, v'' = 0$) band was excited. Second, the OH profile across the y -axis of the burner (i.e., after the burner was rotated by 90°) was obtained using the same line imaging method described for laser absorption. The measured trapping was compared to estimates based on either a *thermal* or a *nonthermal* (i.e., *frozen*) rotational population distribution in $v' = 0$ (for calculating f_J as discussed above). It was also assumed that T was 2,150 K and remained constant across the burner. For the *thermal* assumption, $J' = 0.5\text{--}20.5$ in $v' = 0$ was considered.

Figure 2a plots the measured relative OH signal (solid circle symbols) against laser-probing location along the burner y -axis (i.e., the first step described above). The detailed OH profile (empty diamond symbols) obtained after the burner was rotated (i.e., the second step described above), is plotted on the secondary vertical axis as a reference. Note that in line imaging, fluorescence is assumed to be subject to the same amount of trapping (vs. x , a reasonable assumption since the main flow region is square). The measured fluorescence (solid circle symbols) has been rescaled to match the OH profile at $y = -9$ mm (assuming that at this location trapping is negligible). The calculated relative fluorescence signal (solid and dashed

lines labeled as “Nonthermal” and “Thermal”, respectively) was obtained by multiplying the OH profile across the y -axis (i.e., $S_f(y)$) by the estimated total fluorescence trapping at that location. As can be seen in Fig. 2a, for this particular transition, results from the two different trapping calculation methods are barely distinguishable and both match well with the measured distribution of fluorescence. A larger disagreement can be found between *thermal* and *nonthermal* estimations for transitions with J' levels that are not near the peak of thermal distribution of $v' = 0$. This is demonstrated in Fig. 2b, in which satellite transitions $R_{12}(6.5)$ and $P_{21}(15.5)$ in the OH $A^2\Sigma^+ \leftarrow X^2\Pi$ (0,0) band were used for trapping estimation under the same conditions described for Fig. 2a, using the *nonthermal* assumption. Since the result based on *thermal* assumption is transition independent, it is the same as in Fig. 2a (dashed line). It is evident that the discrepancies between both of the *nonthermal* calculations (labeled by their transition assignments) and the *thermal* one are much larger than in the case shown in Fig. 2a, especially for $P_{21}(15.5)$, where the *nonthermal* assumption predicts very small trapping. Such transition-dependent behavior can be easily attributed to the fact that since a highly populated J' state (such as $J' = 8.5$ in the case of $P_{21}(9.5)$) is heavily weighted in the *thermal* distribution, a *nonthermal* distribution (e.g., where only $J' = 8.5$ is excited and populated) does not deviate much from a *thermal* distribution. By contrast, the *nonthermal* assumption may significantly underestimate trapping for weakly populated J' states (such as $J' = 14.5$ in the case of $P_{21}(15.5)$). The actual trapping effect for $P_{21}(15.5)$ is likely in between the extremes depicted by the two limits shown in Fig. 2b.

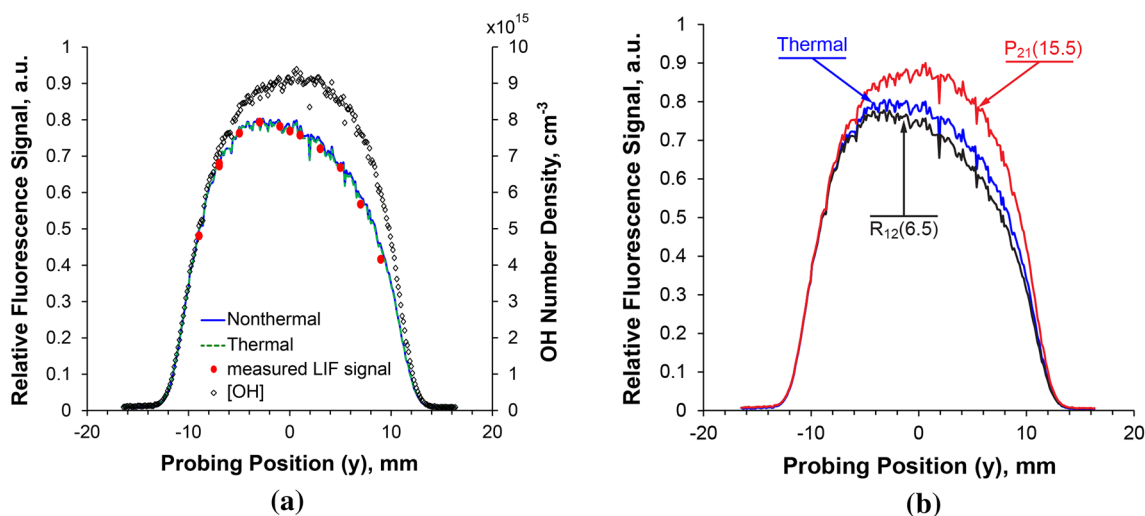


Fig. 2 Effect of fluorescence trapping on LIF signal along its travel path in the near-stoichiometric CH_4 -air Hencken flame. **a** Comparison between measured and estimated fluorescence trapping for the satellite transition $P_{21}(9.5)$ in the OH $A^2\Sigma^+ \leftarrow X^2\Pi$ (0,0) band.

b Estimated fluorescence trapping for satellite transitions $R_{12}(6.5)$ and $P_{21}(15.5)$ in the OH $A^2\Sigma^+ \leftarrow X^2\Pi$ (0,0) band. The laser beam was aligned to be 25 mm above the burner surface

4.3 Laser attenuation

In this work, we consider laser attenuation from a more general point of view. It can be shown that, by taking into account laser absorption (Beer's law) during the derivation of LIF expression, one would arrive at Eq. (3) with an overlap integral $g(v_L)$ as this:

$$g(v_L) = \int_{-\infty}^{+\infty} g_a(v) \cdot \exp[-hv_0 g_a(v) f_B n_{OH} L_{abs}(x) b_{lu}] \cdot g_L(v_L - v) dv, \quad (7)$$

where g_a and g_L are the absorption lineshape and laser lineshape (assumed Gaussian in this work), respectively. It is a common practice in the literature to correct laser intensity attenuation by directly applying Beer's law. This approach, however, does not account for the distortion imposed on the laser lineshape by the absorption profile, as is clearly shown in Eq. (7). Such distortion is most pronounced when the linewidth of the excitation laser is broad compared with that of the absorption. The laser transmittance in our work is thus defined as the ratio between Eq. (7) and that of a normal overlap integral (without the exponential term).

Figure 3 plots the laser transmittance at the transition center (i.e., $v_L = v_0$) along the laser beam propagation direction (along x -axis), calculated based on the measured OH concentration profile (empty diamond symbols) and with $T = 2,150$ K. The laser linewidth used to calculate the transmittance was 0.75 cm^{-1} , estimated for the UV beam from the LIF setup at OSU. As shown in Fig. 3, for relatively strong transitions such as the $R_1(4.5)$ line in the OH $A^2\Sigma^+ \leftarrow X^2\Pi(0,0)$ band, the attenuation can approach 15 % at the center of the flame (where the LIF signal was sampled). Laser attenuation, if not corrected for, may also introduce considerable error in LIF thermometry, since weak transitions (e.g., from high J'') experience less attenuation than from stronger ones (e.g., from low J''), as evident in Fig. 3. For transitions in the (1,0) band, however, the effect of the laser attenuation in this specific case may be negligible (depending on the $n_{OH} \cdot L_{abs}(x)$ product), as long as strong transitions (such as in the Q-branch) are avoided.

It is worth noting that when the laser linewidth is narrower or comparable to the absorption linewidth, laser transmittances based on Eq. (7) and direct Beer's law are nearly identical. On the other hand, if the laser linewidth is much broader than the absorption linewidth, laser attenuation may be underestimated significantly without using Eq. (7) (e.g., by $\sim 8\%$ for $R_1(4.5)$ and $\sim 16\%$ for $Q_1(9.5)$ in the (0,0) band at the peak of the transition at $x = 0$ at our flame conditions). Also note that laser attenuation calculated using Eq. (7) is not significantly affected by the uncertainty in the estimated laser linewidth.

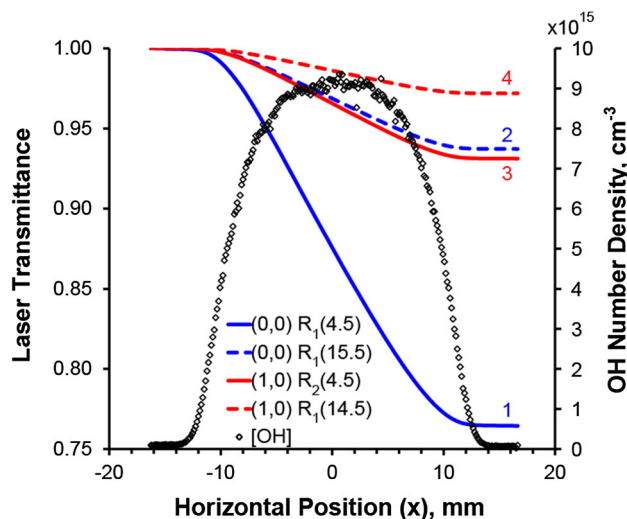


Fig. 3 Calculated laser attenuation in the near-stoichiometric CH_4 -air Hencken flame. The OH concentration profile (empty symbols) is taken from Fig. 2. The solid lines represent laser transmittance calculated at the transition center for (1) (0, 0), $R_1(4.5)$; (2) (0, 0), $R_1(15.5)$; (3) (1, 0), $R_2(4.5)$; (4) (1, 0), $R_1(14.5)$ in the OH $A^2\Sigma^+ \leftarrow X^2\Pi$ electronic system. The laser beam was aligned to $y = 0$ of the burner axis and was 25 mm above the burner surface

4.4 Excitation scans

In order to minimize the effect of the laser linewidth, excitation scans were performed across various transitions (at OSU), and the spectrally integrated LIF spectra were used to derive T and n_{OH} . It is easy to see that the laser lineshape function g_L in the overlap integral [Eq. (7)] drops out when fluorescence signal S_f [Eq. (2)] is spectrally integrated (since the spectral integral of g_L is normalized to 1). For the majority of the measurements, the laser pulse energy was attenuated to about $0.2 \mu\text{J/pulse}$, mainly due to low signal-saturation threshold of the PMT system (but also to insure linear excitation). The tuning of the laser was set to a step size of 0.0005 nm (at the UV wavelength) with 10 laser pulses per step and a 10-Hz pulse repetition rate. The oscilloscope was programmed to integrate both waveforms of the LIF pulse (from the PMT) and the laser pulse energy (from the photodiode) for each laser shot. The median of the 10 shots at each tuning step was used to represent the signal at that laser frequency. A sample excitation spectrum across the $R_1(4.5)$ line in the OH $A^2\Sigma^+ \leftarrow X^2\Pi(0,0)$ band is shown in Fig. 4 (empty symbols). The LIF spectrum shown in Fig. 4 has been corrected for laser attenuation following the method described in Sect. 4.3.

Due to the broad linewidth used for excitation, neighboring transitions may not be completely resolved (see Fig. 4). In order to properly integrate each individual transition, a Voigt function was used in a least-squares

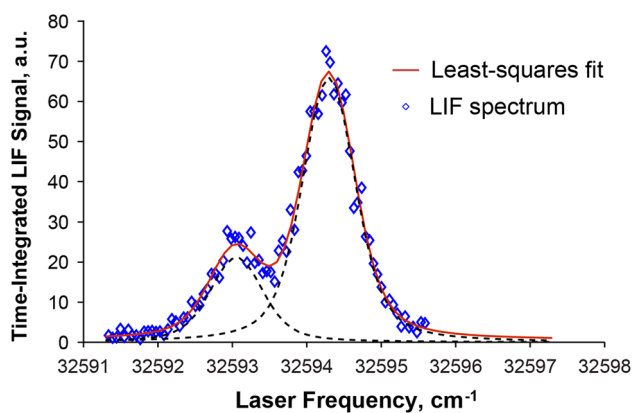


Fig. 4 Sample Voigt profile fitted to an experimental LIF excitation spectrum taken by tuning the laser across $R_1(4.5)$ and $Q_{21}(4.5)$ lines in the OH $A^2\Sigma^+ \leftarrow X^2\Pi$ (0,0) band in the near-stoichiometric CH_4 -air Hencken flame. The laser beam was aligned to $y = 0$ of the burner axis and was 25 mm above the burner surface. The solid line is the Voigt fit for the experimental spectrum (symbols). The dashed lines are individual transitions extracted from the Voigt fit

fitting routine to separate blended transitions. A sample fit is shown as the solid line in Fig. 4. The fitting routine consists of an offset function (i.e., a constant) and a linear combination of individual Voigt profiles representing each transition. The location of each transition is fixed relative to each other by theoretical spectral intervals between transition centers. The magnitude of each transition is determined by a combination of f_B , b_{lu} and a coefficient that considers the quantum yield and scaling against the experimental LIF spectrum. Due to uncertainties in laser linewidth and transition-dependent quantum yield, this program was only used as an aid for spectrum integration. Therefore, all fitting parameters were left freely adjustable. After the fit, individual transitions can be extracted from the superposition of Voigt profiles (with the offset, attributed to background and Rayleigh scattering, subtracted), as illustrated by the dashed lines in Fig. 4. By performing the Voigt fit, each transition can be integrated over the same spectral range, which was chosen to be $\Delta\nu = \pm 10 \text{ cm}^{-1}$ around the transition center to encompass the entire spectrum.

5 OH LIF thermometry

It is well recognized that temperature measurements employing two-line and multi-line OH LIF can be affected by transition-dependent quenching [34] and laser attenuation [35]. In a collision-free setup (e.g., a small temporal collection window is imposed on the LIF pulse), significant error may be introduced if the effect of J' -dependent radiative decay is ignored (since emission largely comes from the directly populated levels) [15]. As a focus of this

work, we will analyze in detail the impact of signal corrections for transition-dependent effects (as described in Sect. 4) on OH LIF thermometry.

For (0,0) excitation, temperatures were derived based on three treatments of the LIF signal: (1) *none* (T_N), wherein no signal correction was applied; (2) *thermal* (T_T), wherein the signal was corrected assuming fully rotationally equilibrated $v' = 0$; (3) *nonthermal* (T_{NT}), wherein the signal was corrected assuming no RET. Both *thermal* and *nonthermal* treatments considered laser beam attenuation and transition-dependent quantum yield (which combines effects of transition-dependent radiative decay rate and fluorescence trapping). Figure 5a shows an example of the *nonthermal* treatment; here, the spectrum was generated by continuously tuning the dye laser across 14 transitions in the R-branch of the OH $A^2\Sigma^+ \leftarrow X^2\Pi$ (0,0) band. Each transition can be distinguished based on the fitting result and then integrated separately without interference from neighboring transitions. However, the $R_2(10.5)$ and $R_1(14.5)$ lines (at about $32,585 \text{ cm}^{-1}$) are *blended* and thus excluded from further analysis. Satellite transitions were discarded for a similar reason. An example of a Boltzmann fit is given in Fig. 5b. The best-fit value for the *nonthermal* treatment is thus $T_{NT} = 2,160 \pm 61 \text{ K}$ with $R^2 = 0.9952$ (uncertainty is 95 % confidence interval). Results using the different *treatments* for (0,0) and (1,0) excitation at both $y = 0 \text{ mm}$ (center of the flame) and $y = -7 \text{ mm}$ (near front edge of the flame, refer to Fig. 1) are summarized in Table 1 and discussed in more detail below.

For *nonthermal* versus *thermal* corrections, since the electronic quenching rate was assumed to be J' independent (see Sect. 4.1), the effects of transition-dependent quantum yield come from the calculated total radiative decay rate and fluorescence transmittance, as explicitly shown in the expression of the quantum yield ϕ_J (i.e., Eq. (4)). Since transition-dependent radiative decay rate and fluorescence transmittance, i.e., $A_{v'=0, J'}^{v'=0, J'}$ and $\text{Tr}_{v'=0, J'}^{v'=0, J'}$ (which is part of $\varepsilon_{v'=0, J'}^{v'=0, J'}$), are the same regardless of the assumptions concerning the population distribution in v' , all the differences can be attributed to f_J (see Eq. (4)). When f_J is assumed to be that of a Boltzmann distribution at the flame temperature (i.e., *thermal* assumption), the total radiative decay rate, and fluorescence transmittance are the same for all excitation transitions used in T inference. For the *nonthermal* correction, fluorescence from low- J' levels generally suffers more trapping than those originating from high- J' levels (since the corresponding J'' levels are sparsely populated), leading to a lower inferred temperature (compared with the *thermal* correction). On the other hand, the total radiative decay rate (i.e., $A_{v'=0, J'}$ in Eq. (4)) decreases with increasing J' [36], resulting in a higher inferred T . For excitation transitions

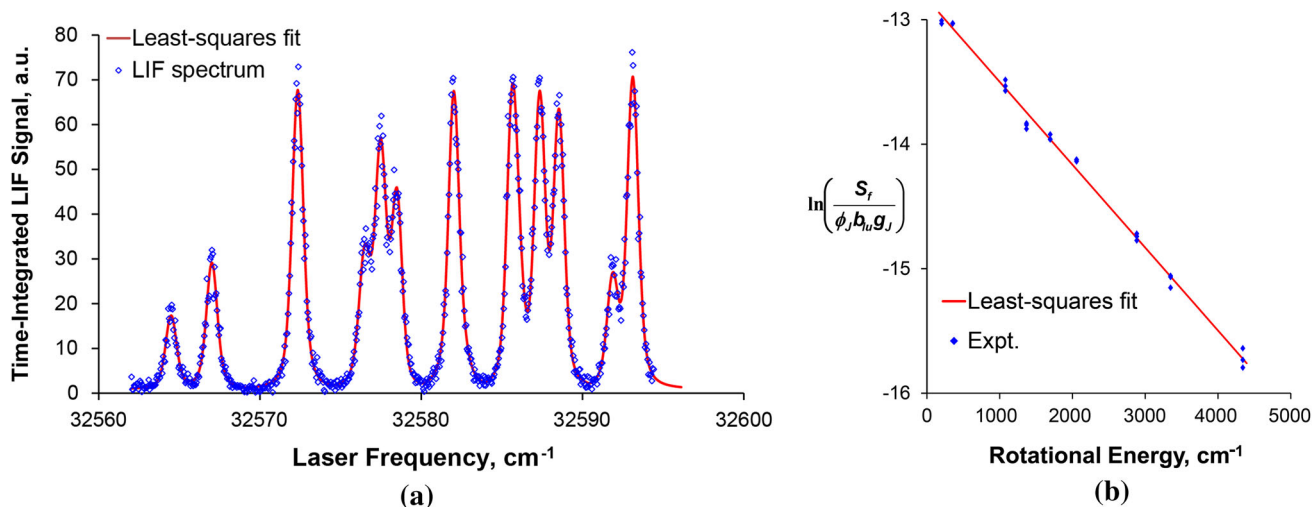


Fig. 5 **a** Sample LIF excitation spectrum with transitions in the R-branch of the OH $A^2\Sigma^+ \leftarrow X^2\Pi$ (0,0) band and its Voigt fit. **b** Temperature inference with Boltzmann fit of integrated LIF spectra

used here, the relative difference between transitions with the lowest and highest fluorescence trapping ratio (for *nonthermal* correction) is $\sim 15\%$ at $y = 0$ mm (total trapping was estimated as 18.4 % for $R_1(4.5)$ and 3.2 % $R_1(15.5)$). A much smaller difference of less than 5 % can be found at $y = -7$ mm (total trapping was estimated as 5.3 % for $R_1(4.5)$ and 0.94 % for $R_1(15.5)$). In comparison, the difference in total radiative decay rate is more than 20 % across the range of J' levels used here. Therefore, the net outcome of the *nonthermal* correction is $T_{NT} > T_T$. The discrepancy between T_{NT} and T_T is much more pronounced close to the edge of the flame ($y = -7$ mm), due to significantly weaker fluorescence trapping (such that the J' dependence in radiative decay rate is not sufficiently mitigated). For *none* versus *thermal* treatments, since laser attenuation lowers the LIF signal from low- J' transitions, $T_N > T_T$ (for *thermal* treatment, total radiative decay as well as fluorescence trapping is J' independent).

For (1,0) band excitation, one additional case (*nonthermal-f*, with “NTF” subscript) with a WG305 filter was examined at $y = 0$ mm. For the directly excited state ($v' = 1$), *thermal* and *nonthermal* corrections are defined the same way as above. However, a common assumption was used for both correction methods: $v' = 0$, which populated through VET, is completely thermalized at the flame temperature. This assumption is backed by reported experimental observations that $v' = 0$ populated by VET exhibits a near thermal (albeit “hotter”) population distribution and carries only a weak memory of the directly excited J' level [37, 38]. Other supporting evidence may be found in Ref. [14], in which electronic quenching and VET were measured by a picosecond laser system in a similar atmospheric-pressure CH_4 -air flame to the one

extracted from (a). The laser beam was aligned to $y = 0$ of the burner axis and was 25 mm above the burner surface, in the near-stoichiometric CH_4 -air Hencken flame

used here. It was observed that $v' = 0$ “thermalizes” to a distribution characteristic of a T about 500 K higher than the actual value. Since the *thermal* distribution varies little in the range of 2,000–3,000 K for $v' = 0$, the *thermal* assumption for $v' = 0$ is not expected to introduce significant error.

Notice that both *none* and *thermal* treatments give very similar values, with T_N being slightly higher, which is consistent with result with (0,0) excitation. This is caused by significantly weaker transition strength found in the (1,0) band (and hence less laser attenuation, see Fig. 3). The difference between the inferred T for *thermal* and *nonthermal* treatments can be explained the same way as with (0,0) excitation. However, in this case, fluorescence trapping is fairly insignificant, due to the fact that (1,1) emission is only very weakly reabsorbed and that emission from $v' = 0$ is assumed to be thermalized (transition independent). Therefore, the inferred T is mostly influenced by the variance in the total radiative decay rate for $v' = 1$ (which raises the inferred T under the *nonthermal* assumption, as explained above). Also seen in Table 1 is a lower T when spectral bias in the WG305 filter is considered (*nonthermal-f*). This can be attributed to the difference in transmittance of the WG305 filter used (34 % increase from 305 to 325 nm, as stated in Sect. 4). The measured filter transmittance for fluorescence increases almost linearly with J' for the transitions used (transmittance for $P_1(2.5)$ fluorescence is about 6 % less than for $R_1(14.5)$), leading to a ~ 50 K reduction in best-fit T when accounted for (compared with the *nonthermal* result).

The impact of various transition-dependent signal treatments on LIF thermometry in the near-stoichiometric CH_4 -air Hencken flame is thus summarized as follows:

Table 1 LIF thermometry using excitation transitions in both (0,0) and (1,0) bands of OH $A^2\Sigma^+ \leftarrow X^2\Pi$ in the near-stoichiometric CH₄-air Hencken flame, 25 mm above the burner surface

Excitation	Range of J'	y (mm)	Correction	T (K)
(0,0)	2.5–15.5 ^a	–7	None	1,967 ± 67
			Thermal	1,922 ± 64
			Nonthermal	2,059 ± 77
	3.5–15.5 ^b	0	None	2,189 ± 65
			Thermal	2,113 ± 58
			Nonthermal	2,160 ± 61
(1,0)	2.5–14.5 ^c	–7 (w/o WG305)	None	1,905 ± 62
			Thermal	1,892 ± 62
			Nonthermal	1,983 ± 70
		0 (w/o WG305)	None	2,134 ± 42
			Thermal	2,118 ± 58
			Nonthermal	2,220 ± 51
	0 (w/WG305)	None	None	2,053 ± 56
			Thermal	2,038 ± 57
			Nonthermal	2,194 ± 69
		Nonthermal f	None	2,144 ± 64

^a Including: P₁(2.5), R₂(3.5), R₁(4.5), R₂(6.5), R₂(12.5), R₁(15.5)

^b Including: R₁(3.5), R₁(4.5), R₂(6.5), R₂(7.5), R₂(8.5), R₂(9.5), R₂(11.5), R₂(12.5), R₁(15.5)

^c Including: P₁(2.5), R₂(4.5), R₂(7.5), R₂(8.5), R₁(11.5), R₂(12.5), R₁(14.5)

1. The effect of laser attenuation is most significant using (0,0) excitation and probing at the center of the flame ($y = 0$); it can lower the inferred T ($T_T < T_N$), by ~ 70 K in this work. For (1,0) excitation, $T_T < T_N$ is also found, but the difference (~ 15 K) is less significant.
2. The overall effect of J' -dependent fluorescence trapping and total radiative decay rate is to increase the inferred T ($T_{NT} > T_T$), up to ~ 100 K in this work.
3. Spectral bias by the WG305 filter is not negligible, leading to a lower inferred T ($T_{NTF} < T_{NT}$), by ~ 50 K in this work.

The LIF-based T can be compared to those inferred from laser absorption, $T_{\text{abs}} = 2,170$ and $2,100$ K at $y = 0$ and $y = -7$ mm, respectively. By taking into account statistical uncertainties (95 % uncertainty interval, as listed in Table 1), all values appear to be in reasonable agreement with the corresponding T_{abs} (especially at $y = 0$). These results, however, do not suggest that signal corrections are not necessary for LIF thermometry. Note that when only two transitions are used to infer T , omission of certain signal corrections (while only considering laser attenuation

as is generally the case) may lead to considerable systematic error, as is clearly shown in the best-fit values listed in Table 1.

The major implications of the discussions above for practical applications of LIF thermometry are given below. In mixtures heavily diluted by Ar and He, a thermalized ν' can usually be achieved due to the fact that RET can be significantly faster than electronic quenching at those conditions [11]. These environments may be encountered (or designed) in shock tube experiments and in plasmas, facilitating signal corrections based on the *thermal* assumption for OH LIF. On the other hand, the *nonthermal* assumption may become more suitable in scenarios where a collision-insensitive setup is employed, such as by imposing a short temporal gate to only collect fluorescence signal during laser excitation. In many cases (such as the Hencken flame used in this work), however, the actual situation most likely lies between the *thermal* and *nonthermal* limits. Since it is not always practical to directly simulate the collisional environments due to uncertainty in the constituents and the availability/reliability of literature cross sections, the two bounding assumptions can be used to derive an uncertainty interval. For complex environments such as gas turbine and coal-fired combustors, where signal corrections may be impossible due to unknown temperature and species concentration distributions, OH LIF thermometry may carry considerable error, especially if high OH concentration is expected (i.e., causing significant laser attenuation and fluorescence trapping).

6 Calibration for absolute OH number density

In order to derive absolute OH number density, n_{OH} , based on Eq. (3), the constant term $I\Omega\beta$ must be known. In this work, Rayleigh scattering at the LIF wavelength was used to obtain $I\Omega\beta$, which is an essential part of the governing formula for Rayleigh scattering signal:

$$S_R(\nu_L) = \frac{\varepsilon_R}{hc\nu_L} \left(\frac{\partial\sigma}{\partial\Omega} \right) I\Omega\beta \cdot (NE), \quad (8)$$

where ε_R is the collection efficiency of the Rayleigh scattering, similar to that defined for ϕ_J in Eq. (4); $N = P/kT$ is the gas number density in the laser probe volume (cm^{-3}); E is the laser pulse energy used for Rayleigh scattering measurements (J); $\partial\sigma/\partial\Omega$ is the Rayleigh scattering differential cross section (cm^2/sr), calculated using dispersion relations for depolarization from Ref. [39] and for index of refraction from Ref. [40]. By varying N and/or E , S_R can be plotted against (NE) ; the slope of this relation contains the constant $I\Omega\beta$ needed for LIF calibration.

For the Rayleigh scattering calibration measurement, the original optical alignment for the OH LIF was largely retained, but a small quartz cell was employed (placed above the Hencken burner) such that the laser beam passed through its center; the cell allows accurate characterization of the background scattering, through the setting of P . It is noted that background scattering might also have been measured with He substituted for N_2 or air, since He has a very small $\partial\sigma/\partial\Omega$ (such that one can easily extrapolate to zero differential cross section). The T-shaped cylindrical test cell features CaF_2 Brewster angle windows for beam entrance and exit, and a CaF_2 window, for collecting scattered signal, 90° to the laser beam. The attenuation of the laser beam by the Brewster angle entrance window was negligibly small, and the displacement of the beam (<1 mm) was accounted for by translation of the PMT assembly. The attenuation of S_R due to the CaF_2 detection window was measured to be 7 % (in good agreement with the specification provided by the manufacturer) and was accounted for in deriving n_{OH} . In order to eliminate the effect of detector quantum efficiency, the laser wavelength was tuned to 308 nm, which is close to the center of OH $A^2\Sigma^+ \leftarrow X^2\Pi$ (0,0) band emission. The quantum efficiency of the PMT used in this work varies less than 3 % across the range of 280–330 nm (according to the manufacturer), which covers the entire (0,0) as well as (1,1) and (1,0) emission region. In addition, the same filters (including colored glasses and ND filters) were used for both OH LIF and Rayleigh scattering. Figure 6 shows one set of Rayleigh scattering data in pure N_2 in the calibration cell at room temperature. At $\nu_L = 308$ nm, the differential Rayleigh cross section was calculated to be 5.93×10^{-27} cm^{-2}/sr and 6.07×10^{-27} cm^{-2}/sr for the synthetic air and pure N_2 , respectively. The constant $I\Omega\beta$ was then derived from the slope of the linear relationship between S_R (background subtracted) and the product of N and E as shown in Fig. 6. Multiple runs in both air and pure N_2 were conducted, and the average of the derived constant $I\Omega\beta$ was used to calibrate the relative OH signal.

Additionally, the probe beam was vertically polarized for both OH LIF and Rayleigh scattering measurements. It is well known that fluorescence from laser-excited OH molecules is polarized and anisotropic at early times after excitation [14]. Although depolarization occurs via collisions, fluorescence has been observed to be partially polarized in an atmospheric-pressure flame [41]. By (1) avoiding Q-branch transitions and (2) employing broadband detection, the effect of polarization on the detected fluorescence is expected to be small (i.e., minimized systematic bias toward a certain transition) [41]. Polarization bias associated with the PMT is expected to be <10 %

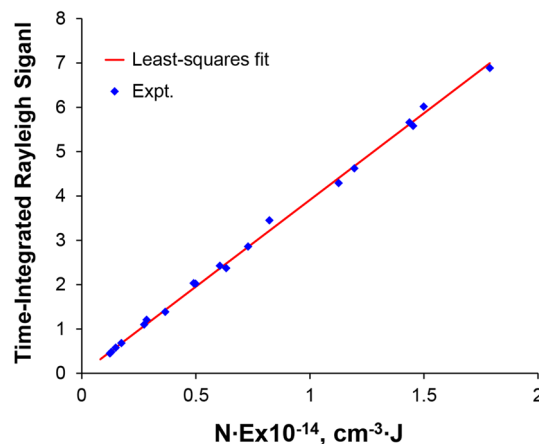


Fig. 6 Sample linear fit of Rayleigh scattering measured in pure N_2 in the calibration cell placed above the burner versus the product of N_2 number density and laser energy. The measurement was conducted at room temperature

(higher efficiency for vertically polarized light, according to the manufacturer), which may result in a slightly higher efficiency when collecting the Rayleigh signal (mostly vertically polarized). Therefore, the derived absolute number density may be underestimated due to such bias, albeit by a small amount (<10 %).

Selected results of absolute OH number densities derived from OH LIF/Rayleigh scattering calibration are given in Table 2, for measurements performed using excitation transitions in both (0,0) and (1,0) bands of the OH $A^2\Sigma^+ \leftarrow X^2\Pi$ electronic system and at both $y = 0$ mm (center of the flame) and at $y = -7$ mm (near the front edge of the flame). T equaling 2,160 and 2,059 K, inferred from LIF thermometry using (0,0) excitation and with *nonthermal* signal correction, was used to calculate f_B for measurements at $y = 0$ mm and $y = -7$ mm, respectively (due to better agreement with T_{abs}). This choice is expected to have fairly limited effect on derived n_{OH} , as for each of the four measurements listed in Table 2, the least temperature-sensitive transition in the range of 2,000–2,300 K was chosen. Note that the values for (1,0) excitation taken with WG305 filter are similar to those taken without (provided that signal attenuation due to the filter is accounted for) and are omitted in Table 2.

Comparing $n_{OH,LIF}$ and $n_{OH,abs}$, the importance of signal correction is apparent (compare *none* with *thermal* and *nonthermal* values), particularly for (0,0) excitation at $y = 0$ mm, with about 33 % underestimation compared with $n_{OH,abs}$ (also given in Table 2) if no correction is applied (this discrepancy is about 42 % for $R_1(3.5)$). Laser attenuation and fluorescence trapping contribute nearly equally to such underestimation, with fluorescence trapping playing a slightly larger role. Additionally, for the selected transitions, the difference between results based on *thermal*

Table 2 Absolute OH number density measured using excitation transitions in both (0,0) and (1,0) bands of OH $A^2\Sigma^+ \leftarrow X^2\Pi$ in the near-stoichiometric CH₄-air Hencken flame, 25 mm above the burner surface

Excitation	Range of J''	y (mm)	Correction	$n_{\text{OH,LIF}}$ (10^{15} cm^{-3}) ^a	$n_{\text{OH,abs}}$ (10^{15} cm^{-3}) ^a
(0,0)	R ₂ (12.5)	−7	None	5.79 ± 0.36	7.1 ± 0.4
			Thermal	6.30 ± 0.39	
			Nonthermal	6.88 ± 0.43	
	R ₂ (9.5)	0	None	6.52 ± 0.05	9.3 ± 0.5
			Thermal	8.42 ± 0.07	
			Nonthermal	8.37 ± 0.07	
(1,0)	R ₁ (11.5) (w/o WG305)	−7	None	6.93 ± 0.78	7.1 ± 0.4
			Thermal	7.19 ± 0.82	
			Nonthermal	7.07 ± 0.80	
	0	0	None	7.81 ± 0.19	9.3 ± 0.5
			Thermal	8.47 ± 0.20	
			Nonthermal	8.77 ± 0.21	

^a Uncertainty is the standard deviation from repeated measurements

and *nonthermal* correction is within the measurement uncertainty (due to the choice of a temperature-insensitive transition, as estimated trapping ratios are similar, see Fig. 2a). The overall uncertainty magnitude in n_{OH} derived from LIF—accounting for run-to-run variations (provided in Table 2), statistical uncertainty in Voigt fit, inaccuracy in measured T , and other uncertainties in rate coefficients, Rayleigh cross section and measured laser energy—was estimated to be <20 %. Taking this uncertainty into account, the agreement between $n_{\text{OH,LIF}}$ and $n_{\text{OH,abs}}$ is good. As mentioned in Sect. 4, it was assumed $Q_1 \approx Q_0$ for cases with (1,0) excitation. With a slightly larger Q_1 (about 10 % more than Q_0 , as reported in [14]), the derived $n_{\text{OH,LIF}}$ from (1,0) excitation will increase by about 7 %. It can be seen that, for absolute OH concentration measurements, choosing a T -insensitive J'' level not only minimizes the effect of T uncertainty but also minimizes differences in fluorescence yield for the two limiting treatments, *thermal* and *nonthermal*, as either method for signal correction gives similar results.

7 OH LIF simulation with LASKIN

The validity of the simple *thermal* and *nonthermal* assumptions has been further examined employing the LASKIN (Laser Kinetics) program [29] to simulate the population distribution in the excited v' state(s). LASKIN incorporates all possible state-to-state energy transfer processes, such as electronic quenching, VET, RET, depolarization, etc., by utilizing cross sections and their J' - and T dependences published by various groups. The specific empirical formulas for J' -dependent quenching and VET (i.e., $Q_{J'}$ for both $v' = 1$ and $v' = 0$, and $V_{10,J'}$ found in Eqs. (4) and (5)) used in this work can be written as:

$$Q(N') = Q(0) \exp[-a(T)N'] \quad (9)$$

for rotational level-dependent quenching for both $v' = 0$ and $v' = 1$, and

$$V_{10}(N') = V_{10}(0)(1 - 0.0343N') \quad (10)$$

for VET from $v' = 1$ to $v' = 0$. (Note that the switch to Hund's case (b) notation is in order for a rotationless state ($N' = 0$) to have exponential term equal to 1.) Although Eq. (9) was thought to overestimate $Q_{J'}$ at low- J' levels [14], it was found to better represent measured fluorescence decay rates by the research group behind LASKIN [16] and was therefore chosen here. The coefficient a in Eq. (9) controls the degree of J' dependence in quenching, which is known to diminish with increasing T as discussed in Sect. 4. The value of a (for $T = 2,150$ K, same for all collision partners) was taken from [16]. The expression for VET was taken from [16], which was demonstrated in fitting of experimental fluorescence spectra from a premixed CH₄-O₂ flame ($T = 2,250$ K). In LASKIN, T -dependent quenching cross sections for various collision partners were calculated using a 2-parameter formula from [13]. The gas composition used in the simulation was the calculated equilibrium composition. The factor $f_{J'}$ (for both $v' = 1$ and $v' = 0$ if any) in the quantum yield expression (Eqs. (4) and (5)) was then derived based on population distributions predicted by LASKIN (time-integrated, as in the experiment). The resulting transition-dependent quantum yield was then used in processing the experimental data to infer T as well as n_{OH} .

Figure 7 shows time-integrated population distributions in the excited vibrational levels following excitations in both (0,0) and (1,0) bands of OH $A^2\Sigma^+ \leftarrow X^2\Pi$, as simulated by LASKIN using conditions found at $y = 0$ (center) of the Hencken flame. Note that population fractions of spin-split states (F_1 and F_2) were added together (hence Hund's case (b) notation is used in the plots). Comparing Fig. 7a and b, for (0,0)-band pumping, it is found that R₂(9.5) excitation results in a more thermalized $v' = 0$ than

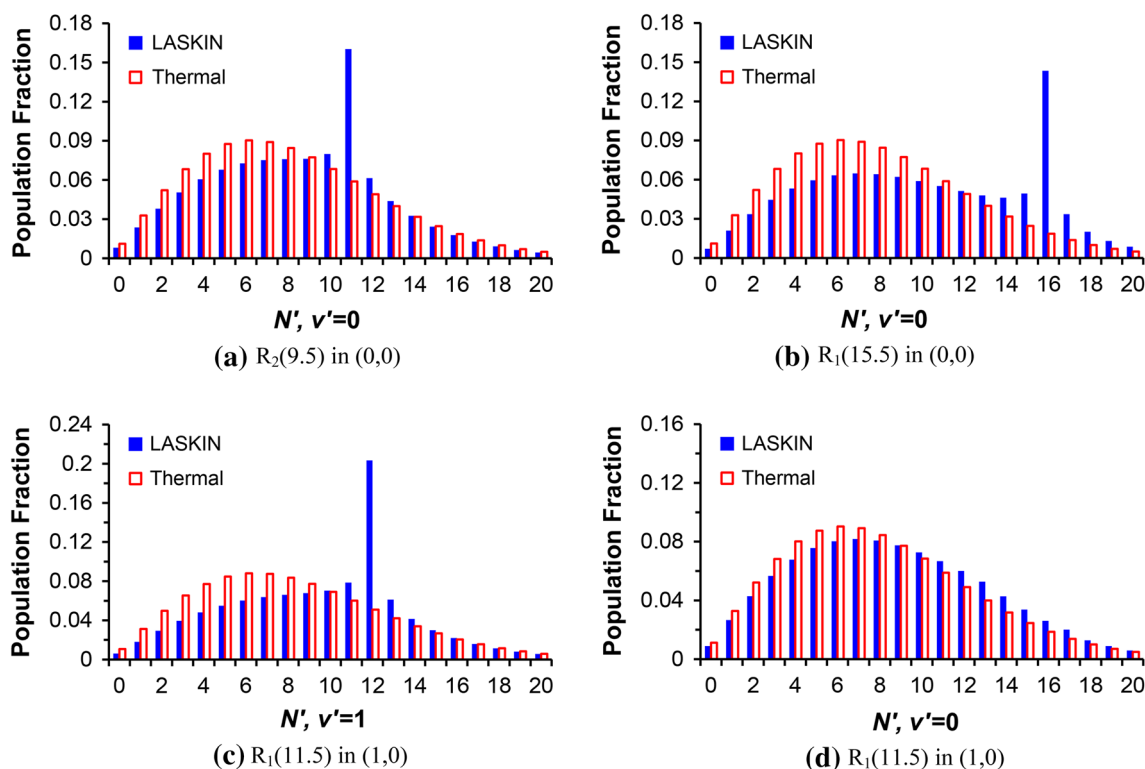


Fig. 7 Time-integrated population distributions in the excited states with excitation transitions in both the (0,0) band and (1,0) band of OH $A^2\Sigma^+ \leftarrow X^2\Pi$, in a near-stoichiometric CH_4 -air Hencken flame, simulated by LASKIN. Conditions used in simulation are equivalent to those found at $y = 0$ mm and 25 mm above the burner surface

with $R_1(15.5)$ excitation, as expected. Figure 7c, d shows population distributions in both $v' = 1$ and $v' = 0$ following the excitation of $R_1(11.5)$ in the (1,0) band. From the simulation, about 60 % of fluorescence originates from $v' = 1$ (not obvious from Fig. 7 since population distributions have been normalized to be compared with thermal distributions). As discussed in Sect. 4, $v' = 0$ populated via VET has been observed to exhibit a “hotter” thermal distribution and retains only a weak memory of directly excited J' in $v' = 1$. This is evident in Fig. 7d, where the population distribution in $v' = 0$ simulated by LASKIN can be fit to a moderately higher temperature of about $T = 2,550$ K.

Figure 8 plots total radiative decay rates and fluorescence transmittance based on the population distribution predicted by LASKIN (such as shown in Fig. 7) as well as simple *thermal* and *nonthermal* assumptions, for all the transitions used in LIF thermometry at $y = 0$ with (0,0) excitation scheme (refer to Table 1 for the full list of transitions). Each transition is represented by its destination (probed) J' level in $v' = 0$ on the x -axis (not distinguishing spin-split states). Observe that calculations based on LASKIN simulation also reveal a J' dependence for both total radiative decay rate and fluorescence transmittance (i.e.,

trapping), though noticeably less steep than estimated based on the *nonthermal* assumption. As expected, the results obtained based on LASKIN fall between those calculated based on either *thermal* or *nonthermal* assumptions (but are closer to the *thermal* case). Also from Fig. 8, it is clear that all three signal corrections converge near the peak of the thermal distribution in $v' = 0$ ($N' = 6$, see Fig. 7a), confirming that signal corrections become less sensitive to the assumptions regarding the collision environment for excitation transitions to these rotational levels. Notice that T -insensitive transitions (with regard to the ground state as described in Sect. 6, such as $R_2(9.5)$ in (0,0) band) satisfy this criterion, albeit not necessarily coinciding with the peak of the thermal distribution in v' . The cases with (1,0) excitation show similar trends as in Fig. 8 and are therefore omitted here.

Derived T and $n_{\text{OH,LIF}}$ based on LASKIN results are summarized in Table 3 for measurements performed at $y = 0$ for both (0,0) and (1,0) excitation. Derived $n_{\text{OH,LIF}}$ matches well with those in Table 2. It should be noted that LASKIN simulations are subject to uncertainties in collision cross sections for RET, VET and electronic quenching of OH $A^2\Sigma^+$. Given that many processes, especially J' -dependent quenching and VET, are not fully understood,

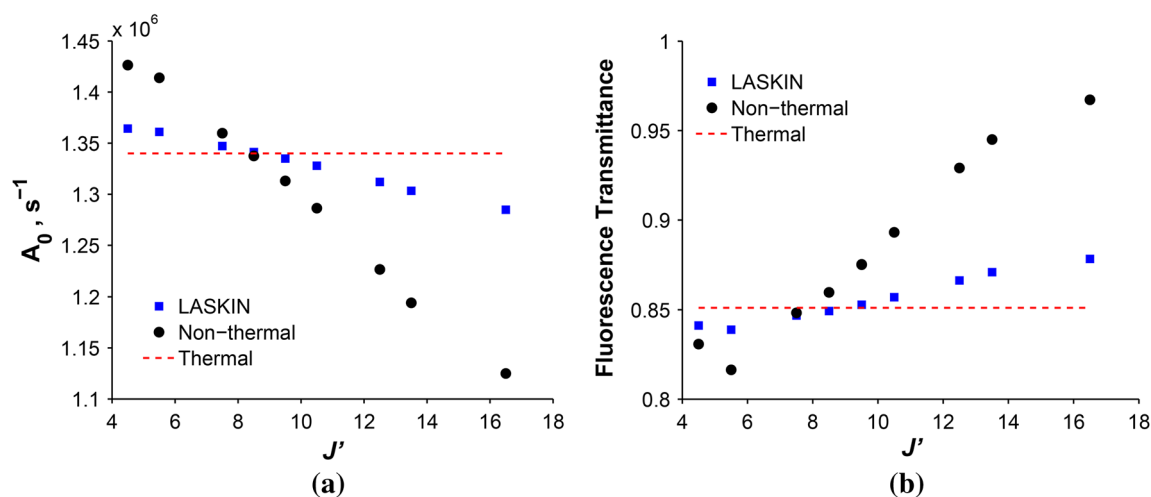


Fig. 8 **a** Radiative decay rate and **b** fluorescence trapping calculated based on time-integrated population distributions in $v' = 0$ predicted by LASKIN with excitation transitions in the OH $A^2\Sigma^+ \leftarrow X^2\Pi$ (0,0) band. Conditions used in simulation are equivalent to those found at $y = 0$ and 25 mm above the burner surface

Table 3 Temperature and absolute OH number density measured using excitation transitions in both (0,0) and (1,0) bands of OH $A^2\Sigma^+ \leftarrow X^2\Pi$ in the near-stoichiometric CH_4 -air Hencken flame, 25 mm above the burner surface. Signal corrections are based on LASKIN simulation

Location	Transition	Correction	T (K)	$n_{\text{OH,LIF}}$ (10^{15} cm^{-3})
$y = 0$	(0,0)/ $R_2(9.5)$	LASKIN	$2,117 \pm 58$	8.44 ± 0.07
	(1,0)/ $R_1(11.5)$ (w/o WG305)		$2,143 \pm 45$	8.58 ± 0.21

LIF signal corrections based on LASKIN simulation should be viewed with caution. Nevertheless, the results demonstrate that *thermal* and *nonthermal* assumptions, albeit simple, can be used to provide reasonable bounds for LIF thermometry. By further employing a T -insensitive transition, T uncertainty will have minimal impact on the derived absolute OH number density. Finally, it is important to emphasize that while this discussion specifically concerns the derivation of an absolute number density from a *Rayleigh scattering calibration*, it is also relevant to any effort to use one condition (e.g., this near-stoichiometric Hencken flame) to calibrate another condition. That is, one would have to enact all of the corrections discussed above to relate the calibration condition to the target condition.

8 Summary

The effects of various corrections to the OH laser-induced fluorescence (LIF) were studied for their impact on derived temperature and OH concentration in an

atmospheric-pressure, near-stoichiometric CH_4 -air flame stabilized on a 25-mm-square Hencken burner. OH rotational temperature was inferred based on excitation scans from both ($v' = 0, v'' = 0$) and ($v' = 1, v'' = 0$) bands. OH LIF signal was corrected by considering transition-dependent laser attenuation and fluorescence quantum yield. Signal corrections were shown to have significant impact on inferred temperature: accounting for laser attenuation lowers the best-fit temperature by as much as ~ 70 K; the overall effect of J' -dependent fluorescence trapping and total radiative decay rate is a net increase in inferred temperature by as much as ~ 100 K. By taking into account statistical uncertainties, the inferred temperatures are roughly in accord with values expected for this burner (i.e., slightly below an adiabatic equilibrium value). In cases where there is less certainty in flame conditions, the approaches discussed can be used to bound the uncertainty in derived temperature and to minimize uncertainty in the absolute OH concentration.

Relative OH concentrations were put on an absolute scale by calibrating the optical collection constant using Rayleigh scattering, demonstrating good agreement with the results from absorption measurements. The results demonstrate that signal corrections are generally necessary for measurements performed in even a small-scale flame: laser absorption can be as much as 20 % for transitions originating from highly populated J'' levels; fluorescence transmittance estimated for a fully thermalized $v' = 0$ (at $T = 2,150$ K) is only about 85 %. Thus, the combined effects of laser absorption and fluorescence trapping would cause considerable bias in the OH number density if not accounted for.

Detailed modeling of OH LIF with excitation from both ($v' = 0, v'' = 0$) and ($v' = 1, v'' = 0$) bands were carried out by implementing the LASKIN program. Simulated time-integrated population distributions in the excited states were used to estimate transition-dependent quantum yield. Temperature and OH number density were inferred from corrected LIF signal based on the simulation, showing consistency with corresponding cases with corrections based on thermalized and *frozen* rotational population distributions, demonstrating their validity as simple bounding approximations treating transition-dependent issues in linear OH LIF.

Finally, it is important to emphasize that the analysis of various signal corrections highlights potential error sources and approaches to their mitigation for either LIF-based (not limited to OH LIF) absolute concentration measurement—regardless of the calibration technique—or temperature measurement, and the approaches and analysis are amenable to the common implementations of LIF.

Acknowledgments This work is supported by the U.S. Air Force Office of Scientific Research MURI “Fundamental Aspects of Plasma Assisted Combustion” Chiping Li—Technical Monitor. The authors would also like to thank the LASKIN group for providing the software.

References

- K. Kohse-Höinghaus, R.S. Barlow, M. Aldén, J. Wolfrum, Proc. Combust. Inst. **30**, 89–123 (2005)
- D.E. Heard, M.J. Pilling, Chem. Rev. **103**, 5163–5198 (2003)
- S. Samukawa, M. Hori, S. Rauf, K. Tachibana, P. Bruggeman, G. Kroesen, J.C. Whitehead, A.B. Murphy, A.F. Gutsol, S. Starikovskaia, U. Kortshagen, J.-P. Boeuf, T.J. Sommerer, M.J. Kushner, U. Czarnetzki, N. Mason, J. Phys. D Appl. Phys. **45**, 253001 (2012)
- P.H. Paul, J. Quant. Spectrosc. Radiat. Transf. **51**, 511–524 (1994)
- A.E. Bailey, D.E. Heard, D.A. Henderson, P.H. Paul, Chem. Phys. Lett. **302**, 132–138 (1999)
- R.A. Copeland, M.J. Dyer, D.R. Crosley, J. Chem. Phys. **82**, 4022–4032 (1985)
- R.A. Copeland, D.R. Crosley, J. Chem. Phys. **84**, 3099–3105 (1986)
- I.J. Wysong, J.B. Jeffries, D.R. Crosley, J. Chem. Phys. **92**, 5218–5222 (1990)
- J.B. Jeffries, K. Kohse-Höinghaus, G.P. Smith, R.A. Copeland, D.R. Crosley, Chem. Phys. Lett. **152**, 160–166 (1988)
- P.H. Paul, J.L. Durant, J.A. Gray, M.R. Furlanetto, J. Chem. Phys. **102**, 8378–8384 (1995)
- P.H. Paul, J. Phys. Chem. **99**, 8472–8476 (1995)
- A. Jörg, U. Meier, R. Kienle, K. Kohse-Höinghaus, Appl. Phys. B **55**, 305–310 (1992)
- M. Tamura, P.A. Berg, J.E. Harrington, J. Luque, J.B. Jeffries, G.P. Smith, D.R. Crosley, Combust. Flame **114**, 502–514 (1998)
- P. Beaud, P.P. Radi, D. Franzke, H.-M. Frey, B. Mischler, A.-P. Tzannis, T. Gerber, Appl. Opt. **37**, 3354–3367 (1998)
- R. Kienle, M.P. Lee, K. Kohse-Höinghaus, Appl. Phys. B **62**, 583–599 (1996)
- U. Rahmann, W. Kreutner, K. Kohse-Höinghaus, Appl. Phys. B **69**, 61–70 (1999)
- C. Cathey, J. Cain, H. Wang, M.A. Gundersen, C. Carter, M. Ryan, Combust. Flame **154**, 715–727 (2008)
- T.R. Meyer, S. Roy, T.N. Anderson, J.D. Miller, V.R. Katta, R.P. Lucht, J.R. Gord, Appl. Opt. **44**, 6729–6740 (2005)
- J. Luque, D.R. Crosley, Appl. Phys. B **63**, 91–98 (1996)
- R.P. Lucht, D.W. Sweeney, N.M. Laurendeau, Combust. Flame **50**, 189–205 (1983)
- J.T. Salmon, N.M. Laurendeau, Appl. Opt. **24**, 1313–1321 (1985)
- C.C. Wang, L.I. Davis Jr., Appl. Phys. Lett. **25**, 34–35 (1974)
- F. Bormann, T. Nielsen, M. Burrows, P. Andresen, Appl. Phys. B **62**, 601–607 (1996)
- M. Versluis, N. Georgiev, L. Martinsson, M. Aldén, S. Kröll, Appl. Phys. B **65**, 411–417 (1997)
- J.A. Coxon, Can. J. Phys. **58**, 933–949 (1980)
- J. Luque, D. R. Crosley, LIFBASE, database and spectral simulation for diatomic molecules, SRI International Report MP-99-009, 1999
- E.C. Rea, A.Y. Chang, R.K. Hanson, J. Quant. Spectrosc. Radiat. Transf. **37**, 117–127 (1987)
- E.C. Rea, A.Y. Chang, R.K. Hanson, J. Quant. Spectrosc. Radiat. Transf. **41**, 29–42 (1989)
- U. Rahmann, A. Bültner, U. Lenhard, R. Düsing, D. Markus, A. Brockhinke and K. Kohse-Höinghaus, LASKIN-A Simulation Program for Time-Resolved LIF-Spectra, Internal Report, University of Bielefeld, Faculty of Chemistry, Physical Chemistry I. <http://pci.uni-bielefeld.de/~laskin>
- N.S. Bergano, P.A. Jaanimagi, M.M. Salour, J.H. Bechtel, Opt. Lett. **8**, 443–445 (1983)
- M. Köllner, P. Monkhouse, J. Wolfrum, Chem. Phys. Lett. **168**, 355–360 (1990)
- R. Sadanandan, W. Meier, J. Heinze, Appl. Phys. B **106**, 717–724 (2012)
- T.M. Muruganandam, B.-H. Kim, M.R. Morrell, V. Nori, M. Patel, B.W. Roming, J.M. Seitzman, Proc. Combust. Inst. **30**, 1601–1609 (2005)
- J.M. Seitzman, R.K. Hanson, P.A. DeBarber, C.F. Hess, Appl. Opt. **33**, 4000–4012 (1994)
- S. Kostka, S. Roy, P.J. Lakusta, T.R. Meyer, M.W. Renfro, J.R. Gord, R. Branam, Appl. Opt. **48**, 6332–6343 (2009)
- J. Luque, D.R. Crosley, J. Chem. Phys. **109**, 439–448 (1998)
- R.A. Copeland, M.L. Wise, D.R. Crosley, J. Phys. Chem. **92**, 5710–5715 (1988)
- L.R. Williams, D.R. Crosley, J. Chem. Phys. **104**, 6507–6514 (1996)
- D.R. Bates, Planet. Space Sci. **32**, 785–790 (1984)
- A. Bucholtz, Appl. Opt. **34**, 2765–2773 (1995)
- P.M. Doherty, D.R. Crosley, Appl. Opt. **23**, 713–721 (1984)